SCIENTIFIC REPORTS

OPEN

2H-NbS$_2$ film as a novel counter electrode for meso-structured perovskite solar cells

Feng Shao[1,2], Zhangliu Tian[2], Peng Qin[2], Kejun Bu[2], Wei Zhao[2], Li Xu[4], Deliang Wang[1] & Fuqiang Huang[2,3]

We report the use of 2H-NbS$_2$ film as a novel counter electrode in perovskite solar cells fabricated with a cold isostatic pressing method. The 2H-NbS$_2$ film, which was prepared through an exfoliation method followed by restacking from Li$_x$NbS$_2$ powder, shows high electrical conductivity of $8.7 \times 10^3 \, S \, cm^{-1}$ and work function of 5.20 eV. The two-dimensional transition metal dichalcogenide was used for the first time as a counter electrode in meso-structured perovskite solar cells. Through this process, we demonstrated a new alternative to noble metals. The perovskite solar cell base on the 2H-NbS$_2$ counter electrode showed an open-circuit voltage of 1.046 V, comparable to that of gold, and a power conversion efficiency of 8.3%.

Perovskite solar cells (PSCs) have been intensively investigated as a promising candidate for the low cost photovoltaic technology since the first report by Miyasaka *et al.* in 2009[1]. Tremendous efforts have been made in the investigation of crystal growth and intrinsic properties of the perovskite materials[2–6] as well as the improvement of device performance and stability[7–9]. The latest certified power conversion efficiencies (PCEs) of the small-area perovskite solar cells (0.0946 cm^2) and mini-modules (36.1 cm^2) have been reported to be 22.1%[10] and 12.1%[11], respectively, approaching those of the commercial polycrystalline silicon, CdTe, and CuIn$_{(1-x)}$Ga$_x$Se$_2$ solar cells[12]. In spite of the rapid advances of the perovskite solar cells, there are concerns with respect to the device degradation and large-scale commercialization[13].

The reactivity of the perovskite material with the back contact has been suggested as an important factor to influence the properties of devices[14–16]. Gold (Au) has been widely used as the counter electrode in PSCs due to its less chemical reactivity, great conductivity and reflectivity, as well as high work function. However, chemical reactions are still observed at the interface[17]. This, together with its high price and the requirement for energy-consuming vacuum processing technique, restrict the further application of noble metals to some extent. To lower the fabrication cost of the counter electrode, it is essential to develop novel alternatives for the replacement of noble metals. The carbon-based materials are promising candidates due to the better stability and low cost[18]. The electrodes with different morphology and composition, such as carbon black[19], graphene[20,21], graphene oxide[22], carbon nanotubes[23,24], carbon paint[25], and carbon cloth[26], have been intensively investigated and the PCEs up to 16% have been achieved[27]. The application of carbon-based electrode in the PSCs provides a new direction for material selection. Up to now, the counter electrode materials used in PSCs are limited to metals and the carbon family. New materials for counter electrode need to be discovered.

The layered transition metal dichalcogenides (TMDs) with the general formula of MX$_2$, where M is a transition metal and X is a chalcogen atom (S, Se or Te), have attracted much attention in recent years due to their excellent electronic properties, great mechanical flexibility, and partial optical transparency. Benefitting from the well-defined crystalline structure with few surface dangling bonds, the TMDs exhibit variable electronic properties such as superconducting (e.g., NbS$_2$), magnetic (e.g., CrSe$_2$), insulating (e.g., BN), topological insulating

[1]Hefei National Laboratory for Physical Sciences at the Microscale, University of Science and Technology of China, Hefei, 230026, China. [2]State Key Laboratory of High Performance Ceramics and Superfine Microstructure, Shanghai Institute of Ceramics, Chinese Academy of Sciences, Shanghai, 200050, China. [3]State Key Laboratory of Rare Earth Materials Chemistry and Applications, College of Chemistry and Molecular Engineering, Peking University, Beijing, 100871, China. [4]Material Laboratory of State Grid Corporation of China, State Key laboratory of Advanced Transmission Technology, Global Energy Interconnection Research Institute, Beijing, China. Correspondence and requests for materials should be addressed to P.Q. (email: qinpeng@mail.sic.ac.cn) or D.W. (email: eedewang@ustc.edu.cn) or F.H. (email: huangfq@mail.sic.ac.cn)
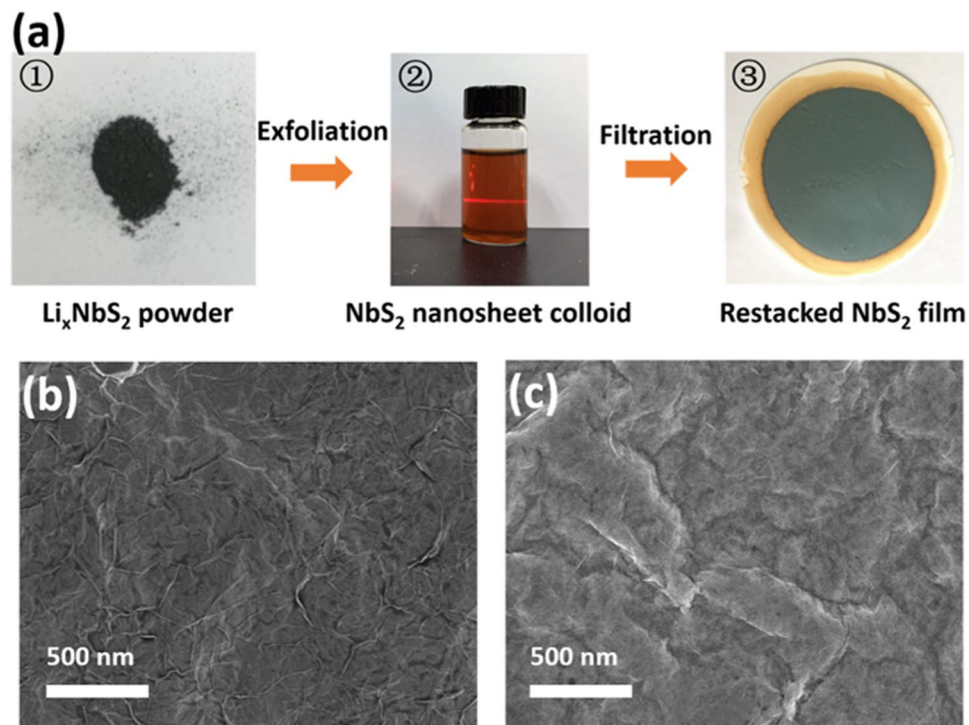
Figure 1. (**a**) The fabrication of NbS$_2$ film from the Li$_x$NbS$_2$ power. Top-view FESEM images of the NbS$_2$ film before (**b**) and after (**c**) the cold isostatic pressing treatment.

(e.g., Bi$_2$Te$_3$), and thermoelectric (e.g., Bi$_2$Te$_3$) phenomena[28]. The weakly bonded atomic layers in these materials facilitate the exfoliation from bulk to thin layers, thus providing a potential application in many fields such as lithium ion battery[29]. In this work, we used a cost-effective and flexibly metallic 2H-NbS$_2$ film as a counter electrode in perovskite solar cells. The cold isostatic pressing (CIP) method was successfully developed instead of the conventional thermal evaporation or solution based printing techniques[30]. The work function of the prepared NbS$_2$ film was measured to be 5.20 eV, matching the highest occupied molecular orbital energy level of the used hole transporting material 2,2′,7,7′-tetrakis(*N*,*N*-di-*p*-methoxyphenylamine)-9,9′-spirobifluorene (spiro-OMeTAD, 5.22 eV)[31,32]. This, together with a high electrical conductivity (8.7×10^3 S cm^{-1}), indicated efficient charge extraction and collection at the counter electrode. The PSC with the configuration of FTO/TiO$_2$/MAPbI$_3$/spiro-OMeTAD/NbS$_2$ has a maximum power conversion efficiency of 8.3% from our measurements. We believe that with further optimization of the material and the fabrication technique, the performance of our devices can be further improved.

Results and Discussion

Figure 1a shows the multi-step process for the preparation of NbS$_2$ thin film[33]. NbS$_2$ powder was firstly synthesized through the conventional solid-state reaction (SSR) from Nb and S[34]. The powder was then reheated with Li$_2$S and Nb for the intercalation of Li cation within the NbS$_2$ layers. Exfoliation of the Li$_x$NbS$_2$ in hydrochloric acid aqueous solution led to the exchange of Li$^+$ with H$^+$, forming a homogeneous NbS$_2$ nanosheet colloid. From the atomic force microscopic (AFM) and high-resolution TEM (HRTEM) images, the prepared NbS$_2$ nanosheets were found to be just one to two layers in most cases with the thickness of around 1.1 nm in the hexagonal lattice structure (Fig. S1a and b). A lattice spacing of 2.90 Å is assigned to the 2H-NbS$_2$ (100) plane. The final NbS$_2$ thin film was fabricated by restacking the prepared nanosheets through vacuum filtration, and the film thickness can be easily tuned by controlling the amount of the colloidal solution. The prepared NbS$_2$ film exhibits many wrinkles as shown in the scanning electron microscopy (SEM) image in Fig. 1b.

The X-ray diffraction (XRD) pattern of the final NbS$_2$ film was measured to check the influence of the Li exfoliation. As shown in Fig. 2a, the (001) plane is shifted from 13.7° to 14.9° due to the decreased inter-planar spacing after extracting the Li$^+$. The only strongest peak at 14.9° confirms the 2H phase and the good lattice orientation after restacking. Figure 2b shows the Hall-effect curve of the prepared NbS$_2$ film with a thickness of 600 nm. By fitting with a linear function with a slope of 5.5×10^{-5} Ω T^{-1}, a carrier concentration of 1.9×10^{21} cm^{-3} is extracted. To further investigate the charge transportation properties, a temperature-dependent resistance variation was measured using a four probe method (Fig. 2c). The prepared NbS$_2$ film exhibits a typical metallic feature with a gradual drop of resistance with the decrease of temperature. A clear superconducting transition is observed when the temperature moves down to 6 K, consistent with previous reports[35,36]. The conductivity of the NbS$_2$ film at 300 K is calculated to be 8.7×10^3 S cm^{-1}, which is lower than that of gold (4.6×10^5 S cm^{-1}). However, it is about 15 times higher than that of the assembled graphene (550 S cm^{-1})[37] and 290 times higher than that of the carbon cloth based electrode (30 S cm^{-1})[26], indicating that our NbS$_2$ films prepared by the SSR method is a good candidate
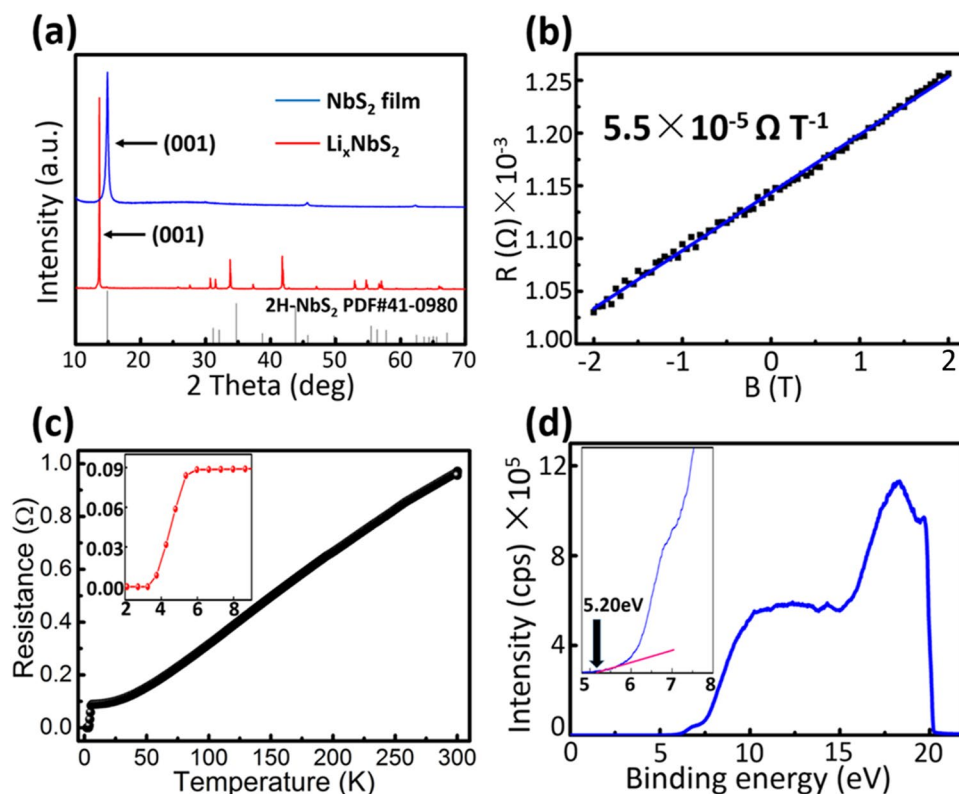
Figure 2. (**a**) XRD patterns of Li_xNbS_2 powder and the NbS_2 film, (**b**) hall resistance (R) as a function of magnetic field (B) at 300 K, (**c**) temperature-dependent resistance curve and (**d**) the UPS spectrum of the prepared NbS_2 film. The thickness of NbS_2 film is 600 nm. The inset in (**c,d**) are the magnifications of local details.

as a counter electrode in PSCs. The DFT calculation was performed to study the electronic structures of $2H\text{-}NbS_2$. No band gap in the bulk $2H\text{-}NbS_2$ was observed, which further confirmed its metallic character (Fig. S2). A work function of 5.20 eV was obtained from the UPS spectrum, slightly higher than that of Au (Figs 2d and S4). Close work functions between NbS_2 and the spiro-OMeTAD hole transporting material (HTM) indicate that the NbS_2 electrode can provide efficient charge separation at the interface.

The exfoliation fabrication process of the device is illustrated in Fig. 3a. The $FTO/TiO_2/MAPbI_3$ electrode was fabricated according to earlier publications[26]. The spiro-OMeTAD solution was then spin-coated on the top of the fresh prepared perovskite layer as a HTM. In the counter electrode part, the prepared NbS_2 film was transferred to the HTM surface, followed by sealing the whole device into a polyethylene envelope under vacuum. The envelope was put into the CIP chamber full of hydraulic oil, pressed with a pressure of 280 MPa at room temperature for a couple of minutes. After this high pressure treatment, the NbS_2 film was tightly plastered onto the spiro-OMeTAD surface (Figs 1c and S3a). No breakages or ruptures were observed under the mechanical pressure treatment from the SEM images. The NbS_2 film was even smoother and more compact comparing with the fresh one (Fig. 1c). Therefore, as a less energy consuming and easy preparation technique, the CIP could be a new method to be used on flexible films for device preparation. The whole device architecture and the energy level diagram are shown in Fig. 3b,c[31,32]. The TiO_2 and spiro-OMeTAD layers work as the electron and hole collector, respectively, with appropriate energy levels for efficient charge extraction.

The influence of NbS_2 thickness on the device performance was investigated. The NbS_2 films with the thickness of 300 nm, 600 nm and 1200 nm were prepared. The best photovoltaic performance was obtained while using the 600 nm film (Fig. S5 and Table S1). It was found that all the performance parameters initially increase with the increase of the NbS_2 film thickness, followed by a drop at film thickness more than 600 nm. Considering the balance between resistance and conductivity, the 600 nm NbS_2 film is chosen in our further studies. For the CIP technique, the pressure is an important factor because the perovskite layer can crack during this process. To check this effect, traditional mesoporous based PSCs with or without spiro-OMeTAD were fabricated and the photovoltaic properties were tested before and after the CIP (280 MPa) treatment. As shown in Fig. S6a and b, no obvious changes were observed after the CIP treatment in both cases. It proves that 280 MPa CIP treatment does not have much effects on the perovskite/HTM layer. A lower pressure of 100 MPa was tested under the same conditions for comparison. As shown from the statistics data, the higher pressure (280 MPa) is slightly better (Fig. S6d). The sequential operation starting from 100 MPa, followed by 280 MPa for one more time did not make any difference (Fig. S6c).

Figure 4a demonstrates the current-voltage characteristics of one of the best performing devices based on the NbS_2 and Au counter electrodes at a scan rate of $10\,mV\,s^{-1}$. The Au electrode was used as a reference for comparison. The photovoltaic parameters are summarized in Table 1. The reference device based on the Au counter
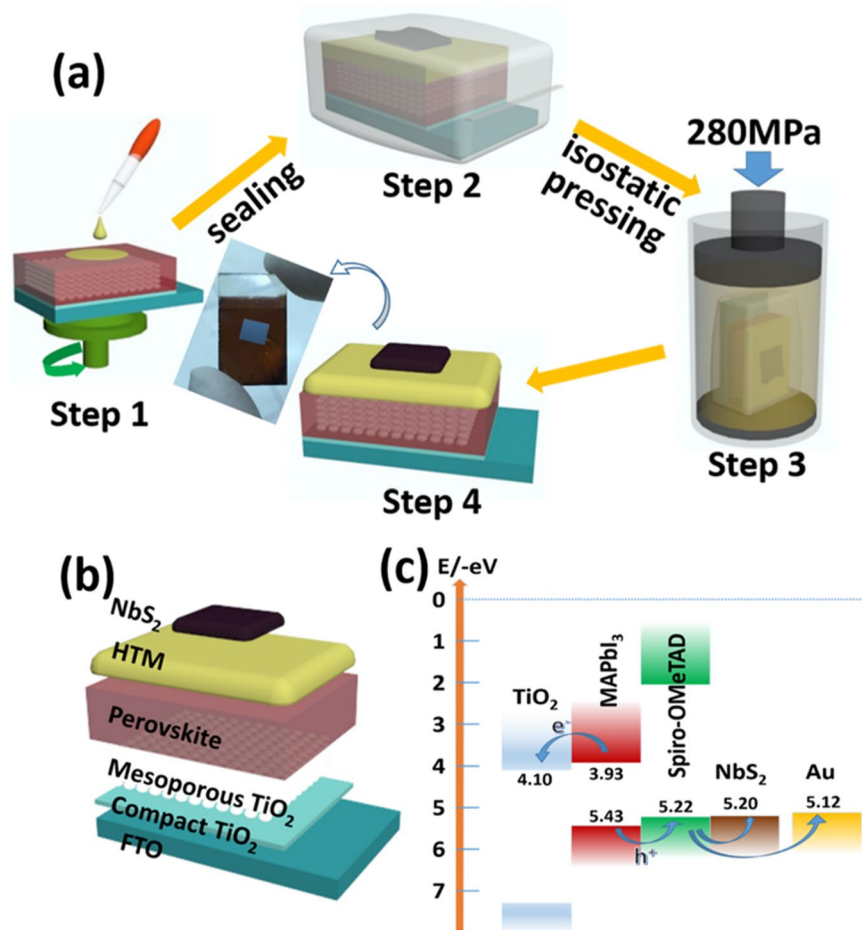
Figure 3. (**a**) Scheme of the device fabrication process, (**b**) the device architecture and (**c**) energy level diagram of FTO/TiO$_2$/MAPbI$_3$/spiro-OMeTAD/NbS$_2$ solar cells.

electrode shows a short-circuit photocurrent density (J_{sc}) of 19.85 mA cm^{-2}, an open-circuit voltage (V_{oc}) of 1036 mV, and a fill factor (FF) of 0.76, resulting in a PCE of 16.37% under standard AM 1.5G illumination. Under the same condition, the NbS$_2$ based device displayed slightly higher V_{oc} of 1046 mV, but lower J_{sc} (14.34 mA cm^{-2}) and FF (0.53), which gave a PCE of 8.31%. The lower J_{sc} and FF are mainly due to the large series resistance related to the NbS$_2$ counter electrode (302.8 Ω) comparing with that of Au (29.4 Ω) either from the NbS$_2$/HTM interface or the NbS$_2$ itself, which then lead to an ineffective charge collection. A small hysteresis is observed in the J-V curves between the forward and reverse scans for NbS$_2$. A slightly low FF leads to a 0.42% drop of PCE in the forward scan. From the incident photon-to-current conversion efficiency (IPCE) spectra, the integrated short-circuit current densities are in agreement with those obtained from the J-V curves (Fig. 4b). The device statistics based on two different counter electrodes over several batches are shown in Figs 4c and S7a. The average PCEs for PSCs based on NbS$_2$ and Au electrodes are 7.22 ± 1.02%, and 15.80 ± 0.45%, respectively (shown in the parenthesis in Table 1). To evaluate the stability of the devices, two unsealed best-performed solar cells based on NbS$_2$ and Au counter electrode were kept in ambient atmosphere (humidity > 50%) at room temperature (24 °C). The J-V curves were measured every 24 h (Figs 4d and S7b). The performance of both cells drops gradually with time, showing 50–60% of their initial value after a period of 7 days.

In summary, we took advantage of a general solid-state strategy to prepare the single-layered 2H-NbS$_2$ nanosheets. Through simple filtration of the nanosheet colloid, the flexible NbS$_2$ film with a high electrical conductivity of 8.7 × 10^3 S cm^{-1} and a work function of 5.20 eV was obtained. The cold isostatic pressing method was firstly used to combine the prepared NbS$_2$ film over the organic hole transporting layer for the preparation of perovskite solar cells. Based on this new counter electrode, the device showed a power conversion efficiency of 8.3% in our tests, and a comparable V_{oc} (1046 mV) comparing with that of gold. The two-dimensional transition metal dichalcogenide film is used as a counter electrode in perovskite solar cells, avoiding the conventional use of expensive noble metals and the high-energy consuming thermal evaporation process. Although both the TMD materials and the isostatic pressing technique need to be further optimized to improve the performance, this method provides an alternative way for the selection of new type of electrodes for the photovoltaic devices.
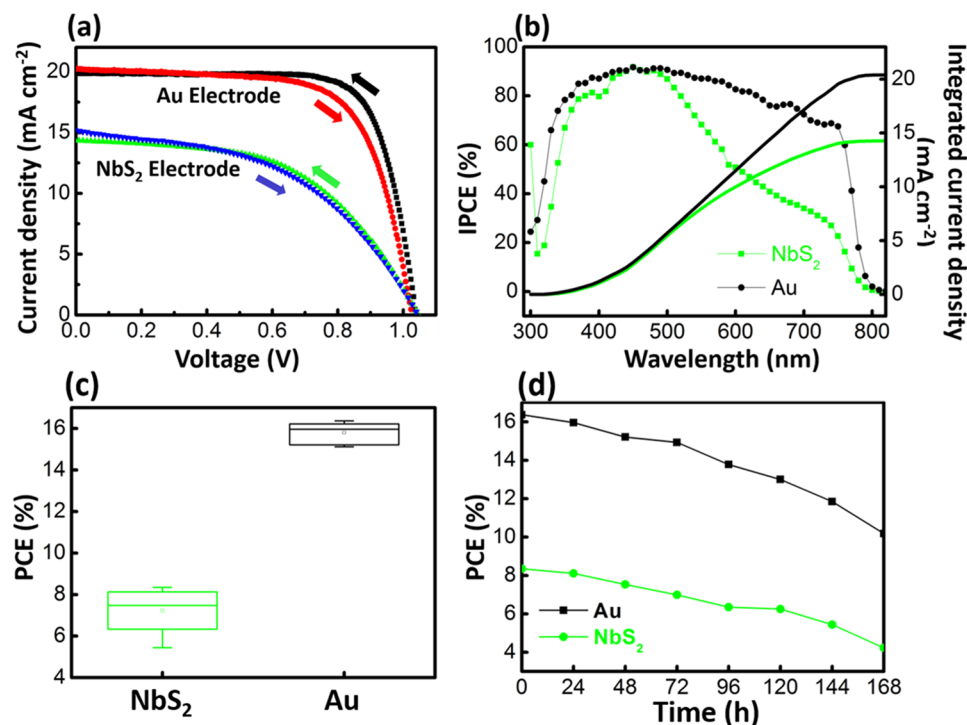
Figure 4. (**a**) Current-voltage (*J-V*) curves of the PSCs using NbS$_2$ and Au as the counter electrode, measured by the forward and reverse scans under AM 1.5 full sun illumination. (**b**) The IPCE spectra of the corresponding devices. The integrated photocurrents calculated are 14.26 and 20.39 mA cm^{-2} for NbS$_2$ and Au, respectively. (**c**) Statistics of PCE. Each box represents the distribution of 10 devices prepared under the same conditions. (**d**) Degradation of PCE of the unencapsulated two best-performed devices under the ambient condition at room temperature (24 °C).

Sample	Scan Direction	V_{oc} (mV)	J_{sc} (mA cm^{-2})	FF	η (%)
Au Electrode	Reverse	1036 (1.039 ± 0.006)	19.85 (19.89 ± 0.37)	0.76 (0.73 ± 0.02)	16.37 (15.80 ± 0.45)
	Froward	1025	20.26	0.68	14.76
NbS$_2$ Electrode	Reverse	1046 (1.020 ± 0.031)	14.34 (14.11 ± 1.57)	0.53 (0.48 ± 0.06)	8.31 (7.22 ± 1.02)
	Forward	1043	15.13	0.48	7.89

Table 1. The photovoltaic parameter of the perovskite solar cells based on NbS$_2$ and Au counter electrode under AM 1.5 G illumination. The average values shown in parentheses were obtained from 10 devices respectively. The active area of the devices is 0.16 cm^2.

Methods

NbS$_2$ film preparation. The NbS$_2$ powder was synthesized by heating the stoichiometric ratio of niobium (99.8%, Alfa Aesar) and sulfur (99.999%, Alfa Aesar) in an evacuated quartz tube at 900 °C for 20 h[33]. The prepared NbS$_2$, together with Li$_2$S and Nb in a molar ratio of 3:2:1, were reheated through solid state reaction at 800 °C for 10 h, for the preparation of Li$_x$NbS$_2$. The NbS$_2$ nanosheets were obtained by chemical exfoliation of Li$_x$NbS$_2$ in the hydrochloric acid (HCl) aqueous solution. In a typical exfoliation process, 30 mL of 1 M HCl was added to 200 mL of water. Then, 5 mg of Li$_x$NbS$_2$ was added. After ultrasonication and stirring for 15 min, the homogeneous NbS$_2$ nanosheet colloid was obtained without any sediments inside, which was dialyzed several times to remove the impurities. The final NbS$_2$ film was obtained through vacuum filtration of the prepared NbS$_2$ nanosheets colloid using a PES (Sterlitech, Kent, WA) filter paper. In a typical experiment, 200 mL NbS$_2$ solution with the concentration same as above led to a membrane thickness of about 300 nm.

Fabrication of the Perovskite Solar Cells. The chemically etched (zinc powder and 4 M HCl) FTO conducting glass was sequentially cleaned by 2% Hellmanex water solution, deionized water, ethanol, and acetone. A 30–50 nm compact TiO$_2$ layer was then deposited by spray pyrolysis at 450 °C from a precursor solution of titanium diisopropoxidebis(acetylacetonate) in anhydrous ethanol, using oxygen as the carrier gas. The mesoporousTiO$_2$ layer was prepared by spin coating the TiO$_2$ paste (Dyesol 30NRD, dilute 7 times in EtOH) at 4000 rpm for 20 s, followed by sintering at 500 °C for 30 min in air. The mixture of methylammonium iodide

(MAI, Dyesol) and PbI_2 (TCI) was dissolved in dimethyl sulfoxide (DMSO) with a molar ratio of 1:1.05. After stirring at 70 °C for 1 h, the precursor solution was spin-coated in a two-step procedure at 1000 and 7000 rpm for 10 and 40 s, respectively. During the second step, 200 μL of 3α-Trifluorotoluene was poured on the spinning substrate 15 s before the end of the procedure. The substrates were then annealed at 100 °C for 1 h in a nitrogen filled glove box. The HTM solution, consisting of 0.06 M Spiro-OMeTAD, 0.03 M bis(trifluoromethylsulphonyl)-imide lithium salt (Li-TFSI, Sigma-Aldrich), 0.006 M tris(2-(1H-pyrazol-1-yl)−4-tert-butylpyridine)−cobalt(III)tris(bis(trifluoromethyl-sulphonyl)imide) (FK209, Dyesol) and 0.2 M 4-tert-butylpyridine (TBP, Sigma-Aldrich) in chlorobenzene, was spin-coated on the top of perovskite layer at 2500 rpm for 15 s. Finally, the NbS_2 film was cut off and transferred on the top of HTM with the help of a cling film. The whole device was sealed in a polyethylene envelope under a vacuum of 0.1 Torr, followed by putting into the hydraulic oil of the isostatic pressing machine for a high-pressure treatment. For comparison, 100 nm Au was deposited on the top of the HTM layer by thermal evaporation as a back contact as the reference.

Measurements and Characterization.

The X-ray diffraction patterns were measured by the Bruker D8 Focus instrument with a monochromatized source of Cu Kα1 radiation ($\lambda = 0.15405$ nm) at 1.6 kW (40 kV, 40 mA). The top-view field emission scanning electron microscopy (FESEM) and transmission electron microscopy (TEM) images were obtained using ZEISS SUPRA 55 microscope and the JEOL 2011microscope (2000 kV), respectively. Topographic imaging of the NbS2 nanosheet was performed using a Bruker Dimension Icon AFM equipped with a NSC14/Cr-Au with a spring force constant of $1−5$ N/m and tip radius < 35 nm. The AFM was operated in the 'tapping' mode. The working point was 20746 nm, scan rate was 1.0 Hz. The temperature-resistance curve and Hall-effect curve of the NbS_2 film with a thickness of 600 nm were characterized by the physical property measurement system (PPMS) of Quantum Design. Temperature variation of the resistance, R (T), was measured using the standard four-probe (in a line, $L_v = 1$ cm, $L_i = 0.8$ cm) technique with the Resistivity model. Hall effect measurements were carried out with Ecopia HMS 3000 setup with a constant current of 0.3 mA in a 4-point configuration measuring an area of 0.5 cm^2. The work function of Au and NbS_2 film were determined by ultraviolet photoemission spectroscopy in Kratos Axis Ultra DLD multitechnique surface analysis system using He I (21.21 eV) photon lines from a discharge lamp with an error about 0.01 eV. The photocurrent density–voltage characteristics of the solar cells were measured using a 1000 W xenon solar simulator (Newport), and the light intensity was calibrated to 100 mW cm^{-2} by a NREL-calibrated Si cell (Oriel 91150). All devices were measured under the ambient air condition at room temperature (24 °C). The active area is 0.16 cm^2 defined by a black mask. The IPCE spectrum was measured by a Newport QE system equipped with a 300 W xenon lamp.

References

1. Kojima, A., Teshima, K., Shirai, Y. & Miyasaka, T. Organometal Halide Perovskites as Visible-Light Sensitizers for Photovoltaic Cells. *Journal of the American Chemical Society* **131**, 6050–6051 (2009).
2. Jeon, N. J. *et al.* Solvent engineering for high-performance inorganic–organic hybrid perovskite solar cells. *Nature Materials* **13**, 897–903 (2014).
3. Dong, Q. F. *et al.* Electron-hole diffusion lengths 175 mu m in solution-grown CH3NH3PbI3 single crystals. *Science* **347**, 967–970 (2015).
4. Motta, C. *et al.* Revealing the role of organic cations in hybrid halide perovskite CH3NH3PbI3. *Nat Commun* **6**, 7026 (2015).
5. Tang, H., He, S. & Peng, C. A Short Progress Report on High-Efficiency Perovskite Solar Cells. *Nanoscale Res Lett* **12**, 410 (2017).
6. Yang, S., Fu, W., Zhang, Z., Chen, H. & Li, C.-Z. Recent advances in perovskite solar cells: efficiency, stability and lead-free perovskite. *Journal of Materials Chemistry A* **5**, 11462–11482 (2017).
7. Konstantakou, M. & Stergiopoulos, T. A critical review on tin halide perovskite solar cells. *Journal of Materials Chemistry A* **5**, 11518–11549 (2017).
8. Li, X. *et al.* A vacuum flash-assisted solution process for high-efficiency large-area perovskite solar cells. *Science* **353**, 58–62 (2016).
9. Chen, W. *et al.* Efficient and stable large-area perovskite solar cells with inorganic charge extraction layers. *Science* **350**, 944–948 (2015).
10. Yang, W. S. *et al.* Iodide management in formamidinium-lead-halide-based perovskite layers for efficient solar cells. *Science* **356**, 1376–1379 (2017).
11. Chen, H. *et al.* A solvent- and vacuum-free route to large-area perovskite films for efficient solar modules. *Nature* **550**, 92–95 (2017).
12. Green, M. A. *et al.* Solar cell efficiency tables (version 50). *Prog Photovoltaics* **25**, 668–676 (2017).
13. Petrus, M. L. *et al.* Capturing the Sun: A Review of the Challenges and Perspectives of Perovskite Solar Cells. *Advanced Energy Materials* **7**, 1700264 (2017).
14. Kato, Y. *et al.* Silver Iodide Formation in Methyl Ammonium Lead Iodide Perovskite Solar Cells with Silver Top Electrodes. *Adv Mater Interfaces* **2**, 1500195 (2015).
15. Zhao, L. F. *et al.* Redox Chemistry Dominates the Degradation and Decomposition of Metal Halide Perovskite Optoelectronic Devices. *Acs Energy Lett* **1**, 595–602 (2016).
16. Li, J., Dong, Q., Li, N. & Wang, L. Direct Evidence of Ion Diffusion for the Silver-Electrode-Induced Thermal Degradation of Inverted Perovskite Solar Cells. *Advanced Energy Materials* **7**, 1602922 (2017).
17. Guerrero, A. *et al.* Interfacial Degradation of Planar Lead Halide Perovskite Solar Cells. *ACS Nano* **10**, 218–224 (2016).
18. Chen, H. & Yang, S. Carbon-Based Perovskite Solar Cells without Hole Transport Materials: The Front Runner to the Market? *Advanced materials* **29** (2017).
19. Wei, Z. H. *et al.* Cost-efficient clamping solar cells using candle soot for hole extraction from ambipolar perovskites. *Energy & Environmental Science* **7**, 3326–3333 (2014).
20. Lang, F. *et al.* Perovskite Solar Cells with Large-Area CVD-Graphene for Tandem Solar Cells. *Journal of Physical Chemistry Letters* **6**, 2745–2750 (2015).
21. Yan, K. *et al.* High-performance graphene-based hole conductor-free perovskite solar cells: Schottky junction enhanced hole extraction and electron blocking. *Small* **11**, 2269–2274 (2015).
22. Wu, Z. W. *et al.* Efficient planar heterojunction perovskite solar cells employing graphene oxide as hole conductor. *Nanoscale* **6** (2014).
23. Habisreutinger, S. N. *et al.* Enhanced Hole Extraction in Perovskite Solar Cells Through Carbon Nanotubes. *Journal of Physical Chemistry Letters* **5**, 4207–4212 (2014).

24. Wei, Z., Chen, H., Yan, K., Zheng, X. & Yang, S. Hysteresis-free multi-walled carbon nanotube-based perovskite solar cells with a high fill factor. *Journal of Materials Chemistry A* **3**, 24226–24231 (2015).
25. Ryu, J. *et al.* Paintable Carbon-Based Perovskite Solar Cells with Engineered Perovskite/Carbon Interface Using Carbon Nanotubes Dripping Method. *Small* **13**, 1701225 (2017).
26. Gholipour, S. *et al.* Highly Efficient and Stable Perovskite Solar Cells based on a Low-Cost Carbon Cloth. *Advanced Energy Materials* **6**, 1601116 (2016).
27. Zhang, F., Yang, X., Cheng, M., Wang, W. & Sun, L. Boosting the efficiency and the stability of low cost perovskite solar cells by using CuPc nanorods as hole transport material and carbon as counter electrode. *Nano Energy* **20**, 108–116 (2016).
28. Duan, X., Wang, C., Pan, A., Yu, R. & Duan, X. Two-dimensional transition metal dichalcogenides as atomically thin semiconductors: opportunities and challenges. *Chem Soc Rev* **44**, 8859–8876 (2015).
29. Di Pietro., B., Patriarca, M. & Scrosati, B. Electrochemical investigation of the lithium-niobium disulphide organic electrolyte rechargeable cell. *Synthetic Metals* **5**, 1–9 (1982).
30. Weerasinghe, H. C., Sirimanne, P. M., Simon, G. P. & Cheng, Y.-B. Cold isostatic pressing technique for producing highly efficient flexible dye-sensitised solar cells on plastic substrates. *Progress in Photovoltaics: Research and Applications* **20**, 321–332 (2012).
31. Kim, H. S. *et al.* Lead Iodide Perovskite Sensitized All-Solid-State Submicron Thin Film Mesoscopic Solar Cell with Efficiency Exceeding 9%. *Scientific reports* **2**, 591 (2012).
32. Zhou, H. *et al.* Interface engineering of highly efficient perovskite solar cells. *Science* **345**, 542–546 (2014).
33. Guo, C. G. *et al.* High-quality single-layer nanosheets of MS2 (M = Mo, Nb, Ta, Ti) directly exfoliated from AMS(2) (A = Li, Na, K) crystals. *Journal of Materials Chemistry C* **5**, 5977–5983 (2017).
34. Jellinek, F., Brauer, G. & Mu¨ller, H. Molybdenum and Niobium Sulphides. *Nature* **185**, 376–377 (1960).
35. Hamaue, Y. & Aoki, R. Effects of Organic Intercalation on Lattice-Vibrations and Superconducting Properties of 2h-Nbs₂. *J Phys Soc Jpn* **55**, 1327–1335 (1986).
36. Wilson, J. A., Di Salvo, F. J. & Mahajan, S. Charge-density waves and superlattices in the metallic layered transition metal dichalcogenides (Reprinted from Advances in Physics, vol 32, pg 882, 1974). *Adv Phys* **50**, 1171-1248 (2001).
37. Wang, X., Zhi, L. J. & Mullen, K. Transparent, conductive graphene electrodes for dye-sensitized solar cells. *Nano letters* **8**, 323–327 (2008).

Acknowledgements

Author Contributions

F.S. and Z.T. designed the experiments, fabricated and measured the solar cells. K.B., W.Z., and L.X. helped with the characterization. P.Q., D.W. and F.H. supervised the project. S.F. and P.Q. wrote the draft of the paper. All the authors contributed to the discussion and revision of the paper.

Additional Information

Supplementary information accompanies this paper at https://doi.org/10.1038/s41598-018-25449-x.

Competing Interests: The authors declare no competing interests.

Publisher's note: Springer Nature remains neutral with regard to jurisdictional claims in published maps and institutional affiliations.